

# Rapid #: -15675566

CROSS REF ID: **2087944**

LENDER: **UUM :: Marriott Library**

BORROWER: **IXA :: Main Library**

TYPE: Article CC:CCG

JOURNAL TITLE: Advanced optical materials

USER JOURNAL TITLE: Advanced Optical Materials

ARTICLE TITLE: "Point-and-Shoot" Synthesis of Metallic Ring Arrays and Surface-Enhanced Optical Spectroscopy

ARTICLE AUTHOR: Rajeeva, Bharath Bangalore

VOLUME: 6

ISSUE: 10

MONTH:

YEAR: 2018

PAGES: 1-7

ISSN: 2195-1071

OCLC #:

Processed by RapidX: 1/23/2020 1:34:32 PM



This material may be protected by copyright law (Title 17 U.S. Code)

---

# “Point-and-Shoot” Synthesis of Metallic Ring Arrays and Surface-Enhanced Optical Spectroscopy

Bharath Bangalore Rajeeva, Zilong Wu, Andrew Briggs, Palash V. Acharya, S. Brett Walker, Xiaolei Peng, Vaibhav Bahadur, Seth R. Bank, and Yuebing Zheng\*

The realization of optically active structures with direct-write printing has been challenging, particularly in spatially constrained microfluidic devices which are essential for point-of-care (POC) applications. The existing techniques are limited by resolution, accessibility, and multistep fabrication constraints. “Point-and-shoot” strategies to achieve site-specific fabrication of optically active Ag rings and on-demand targeted surface-enhanced optical spectroscopy are reported. Stable microbubbles over an Au nanoisland (AuNI) substrate are generated using a continuous-wave laser at low power ( $\approx 0.5 \text{ mW } \mu\text{m}^{-2}$ ). Analytical modeling of bubble generation process substantiates the evolution of ring morphology and its power dependence. The tunable Ag rings exhibit surface plasmon resonances in the mid-IR regime from 3.8 to 4.6  $\mu\text{m}$ , while the AuNI shows visible region response. The Ag ring over the AuNI imparts intensified surface-enhanced Raman spectroscopy (SERS) activity owing to amplified hot spots at Ag ring/AuNI interface. As an example, SERS and surface-enhanced infrared spectroscopy of rhodamine 6G, crystal violet, and 2,4,6-trinitrotoluene molecules, respectively, are demonstrated. The applicability of this technique to perform in situ fabrication and SERS sensing in microfluidic channels is shown. Using a simple in situ approach toward optically active structures, our technique can synergize multiple surface-enhanced optical spectroscopies to facilitate POC applications.

Advancements in the fields of plasmonics and metamaterials have enabled exploration of numerous materials, architectures, and fabrication protocols to achieve multifunctional substrates

B. B. Rajeeva, Z. Wu, X. Peng, Prof. Y. Zheng  
Materials Science and Engineering Program  
Department of Mechanical Engineering  
The University of Texas at Austin  
Austin, TX 78712, USA  
E-mail: zheng@austin.utexas.edu

A. Briggs, Prof. S. R. Bank  
Microelectronics Research Centre  
The University of Texas at Austin  
Austin, TX 78758, USA

P. V. Acharya, Prof. V. Bahadur  
Department of Mechanical Engineering  
The University of Texas at Austin  
Austin, TX 78712, USA

Dr. S. B. Walker  
Electroninks  
3006 Longhorn Blvd #113, Austin, TX 78758, USA

 The ORCID identification number(s) for the author(s) of this article can be found under <https://doi.org/10.1002/adom.201701213>.

DOI: 10.1002/adom.201701213

for surface-enhanced optical spectroscopies.<sup>[1]</sup> Metallic rings are actively explored due to their unique optical, electrical, and magnetic properties.<sup>[2–4]</sup> The metallic ring morphology presents high symmetry and surface area. At the excitation of surface plasmons, uniformly enhanced electric field exists inside the circular cavity, which benefits biosensors,<sup>[5–9]</sup> metamaterials,<sup>[10,11]</sup> surface-enhanced optical spectroscopies,<sup>[12,13]</sup> and other optical applications.<sup>[14,15]</sup> Further, integration of the plasmonic structures with microfluidics is crucial for applications such as microreactors and point-of-care devices.<sup>[16,17]</sup>

Several approaches such as colloidal templating and self-assembly have been applied to fabricate metallic ring-shaped architectures.<sup>[18–20]</sup> Colloidal templating usually consists of multiple steps, including colloidal particle assembly, polishing, metal deposition, and selective etching.<sup>[21]</sup> Scherer and co-workers reported self-organized nanorings arrays based on colloidal silica spheres.<sup>[20]</sup> In contrast to the template-based techniques,

the direct-write process could enable real-time structural configurability, minimal material wastage, and multicomponent integration.<sup>[22]</sup> However, the dominant direct-writing-based approaches such as electron beam lithography<sup>[23,24]</sup> and femtosecond laser writing technique<sup>[25]</sup> still require multistep processes, which involve resist patterning, metal deposition, and selective etching, to achieve the metallic rings. The multistep processes hinder the in situ ring fabrication within the microfluidic channels. Laser-writing with a precursor ink is a viable strategy to exploit the full advantages of direct-writing process for in situ fabrication under various spatial constraints.<sup>[26]</sup> However, existing strategies for in situ synthesis in microfluidic channels have limited control over the structural integrity and morphology of the fabricated micro/nanostructures.

We report a simple “point-and-shoot” technique for single-step site-specific fabrication of Ag rings to realize multiresponsive plasmonic substrates for surface-enhanced optical spectroscopies. The technique involves direct synthesis and immobilization of Ag rings over an Au nanoisland (AuNI) substrate from an Ag precursor ink using a laser-generated microbubble. By using the low-temperature reducible Ag ink and controlling the laser-induced microbubble growth via highly

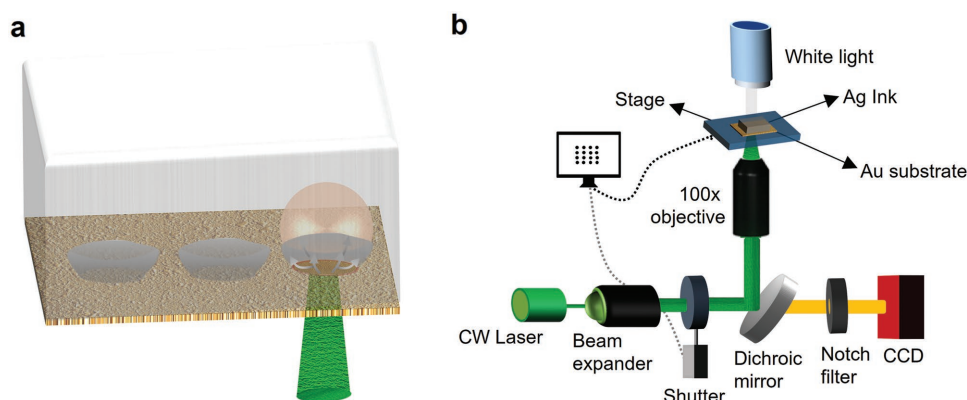


**Figure 1.** a) Illustration of the bubble-mediated fabrication of Ag rings over the AuNI substrate. b) Schematic of the optical setup comprising the synchronized automated stage and optical shutter.

localized optothermal effects, we realize optically active Ag rings with tunable diameters between 1 and 2  $\mu\text{m}$ . The ring morphology is defined by the immobilization of thermally reduced Ag from the precursor along the bubble/water interface. Analytical modeling of the immobilization process demonstrates the dynamics of Ag postnucleation, eventually leading to the formation of the ring structures. We show that the tunable mid-IR and visible responses arise from the Ag rings and the underlying AuNIs, respectively. We employ the multiresponsive Ag ring-AuNI substrate to sequentially perform surface-enhanced infrared spectroscopy (SEIRS) of 2,4,6-trinitrotoluene (TNT) and surface-enhanced Raman spectroscopy (SERS) of rhodamine 6G (R6G) and crystal violet (CV). The above analytes are used as model molecules to establish the multimode response of the substrate. Furthermore, we demonstrate in situ fabrication of Ag rings with a versatile structural and optical control for “point-and-shoot” surface-enhanced optical spectroscopy within a single microfluidic channel.

**Figure 1** depicts the working mechanism and the optical setup for the bubble-mediated Ag ring fabrication. The Ag precursor ink is positioned on the AuNI substrate consisting of a network of Au nanoparticles (NPs) with an average size of  $\approx 30$  nm and an interparticle distance of  $\approx 15$  nm. Direct synthesis and immobilization of Ag structures on the substrate are achieved via photothermal effects of AuNIs upon the excitation of surface plasmons by a continuous-wave laser (532 nm). The laser beam focused on the AuNI substrate results in a highly localized temperature increase due to the nonradiative Landau damping of surface plasmons,<sup>[27]</sup> which generates a size-controllable microbubble.<sup>[28–30]</sup> The thermal gradient around the microbubble induces Marangoni convection, which concentrates the  $\text{Ag}^+$  ions at the bubble surface and thermally reduces the ions into Ag NPs forming a ring-like structure.<sup>[31]</sup> Thus, the process can be divided into two regimes: (i) reduction and nucleation of  $\text{Ag}^+$  ions into Ag NPs, and (ii) bubble growth dynamics leading to an Ag ring. The AuNI substrate is placed on an automated stage synchronized with an optical shutter to achieve site-specific fabrication of the Ag rings.

Our Ag precursor ink has a very low precipitation temperature of  $\approx 85^\circ\text{C}$ , which facilitates the simultaneous reduction and patterning of Ag structures on the AuNI substrate. At relatively lower laser power ( $<0.5\text{ mW }\mu\text{m}^{-2}$ ), conventional photothermal

heating at the AuNI substrate leads to continuous Ag lines with a power-dependent linewidth (**Figure 2a**). The uniform hot spot distribution at the AuNI substrate sustains a stable temperature increase over a large area, which leads to the consistent linewidth of individual Ag lines. Complex patterns such as gammadion arrays and inverted U-structure arrays with sub-micrometer linewidth ( $\approx 0.8\text{ }\mu\text{m}$ ) were also fabricated with the direct-printing technique at the lower laser power (Figure 2b and Figure S1, Supporting Information). With an increased power ( $>0.5\text{ mW }\mu\text{m}^{-2}$ ), the laser beam generates microbubbles, as evidenced in Video S1 (Supporting Information). The Ag precursor is thermally reduced and deposited along the bubble interfaces to form an Ag ring in a single step. By repeatedly generating isolated individual bubbles at predetermined locations, we create an array of Ag rings on the substrate. To limit the growth of the bubble to create small rings of 1–2  $\mu\text{m}$  in diameter, a short stage-waiting time of 350 ms is used at each location. It is worth noting that the high-density uniform particles and hot spots at the AuNI substrate enable the consistent fabrication of the uniform Ag rings. An Ag ring array ( $60\text{ }\mu\text{m} \times 50\text{ }\mu\text{m}$ ) with a 3  $\mu\text{m}$  inter-ring spacing along  $x$  and  $y$  directions is shown in Figure S2 (Supporting Information). As shown in Figure 2c–f, we can control ring sizes by the laser power (see also Video S2, Supporting Information).

Precise control of Ag ring structures and optical responses relies on the ability to instantaneously nucleate and immobilize Ag NPs at high spatial resolution. However, a low viscosity (2 mPa s) of the precursor Ag ink usually limits the printing resolution to several micrometers.<sup>[32]</sup> In our bubble-mediated printing, the plasmon-enhanced localized thermal field over the AuNI substrate confines the active reaction area at the sub-micrometer scale to improve the resolution.<sup>[33]</sup> The bubble also concentrates the  $\text{Ag}^+$  ions at the three-phase contact line via Marangoni convection. The ions are subsequently reduced to Ag according to Equation (1)



High temperature ( $>100^\circ\text{C}$ ) arises from the photothermal effects associated with the dense and uniform plasmonic hot spots at the AuNI substrate.<sup>[28]</sup> The high temperature and ion concentration lead to instantaneous ( $<100$  ms) nucleation of

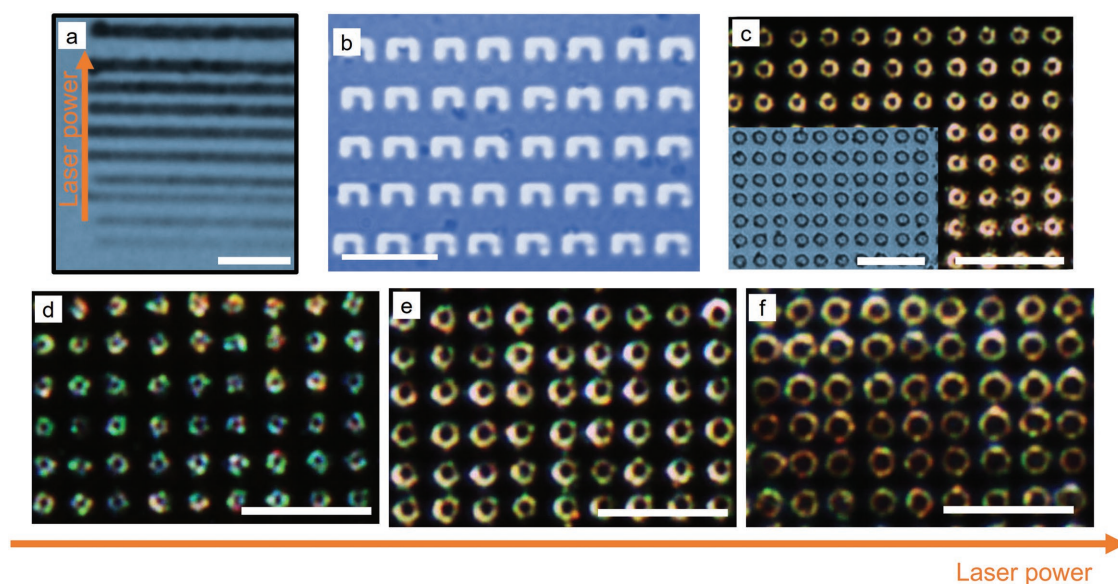


**Figure 2.** a) Fabrication of Ag lines by a laser beam below the bubble-generation threshold power. The linewidth increases when the laser power is increased from 0.2 to 0.5  $\text{mW } \mu\text{m}^{-2}$ . The bubble is observable when the laser beam is at the end of the line. b) Arrays of Ag inverted-U structures fabricated by a laser beam below the bubble-generation threshold power. c) Dark-field optical image of an Ag ring array fabricated at a laser power of 0.75  $\text{mW } \mu\text{m}^{-2}$ . The inset shows the bright-field optical image. d–f) Dark-field optical images of arrays of Ag rings of variable sizes. The incident laser power is d) 0.55, e) 0.81, and f) 0.95  $\text{mW } \mu\text{m}^{-2}$ . The scale bar is 10  $\mu\text{m}$  for all the panels.

Ag. According to classical nucleation theory, the nucleation rate  $R$  is given by

$$R = N_s Z j e^{\frac{-\Delta G}{k_B T}} \quad (2)$$

where  $N_s$  is the density of  $\text{Ag}^+$  ions,  $Z$  is the Zeldovich factor,  $j$  is the rate at which molecules attach for the nucleus to grow,  $\Delta G$  is the critical free energy of nucleation,  $k_B$  is the Boltzmann constant, and  $T$  is the absolute temperature. With the reaction primarily confined to the three-phase contact line, the free energy change for the heterogeneous nucleation is given by<sup>[34]</sup>

$$\Delta G_{\text{hetero}} = \Delta G f(\theta) \quad (3)$$

$$f(\theta) = \frac{1}{2} - \frac{3}{4} \cos\theta + \frac{1}{4} \cos^3\theta \quad (4)$$

where  $\theta$  is the contact angle. The reduced free energy barrier at the bubble/substrate interface leads to the faster nucleation. The higher ion concentration at the interface reduces the critical nucleus radius, leading to the higher-resolution Ag structures.<sup>[34]</sup>

To explain the physics behind the Ag ring formation, we consider the force balance on a single Ag particle following the nucleation event. The particle dynamics is governed by an interplay among the surface tension ( $F_s$ ), pressure ( $F_p$ ), and drag force ( $F_d$ ).<sup>[28,35]</sup> The particle accumulation at the bubble interface is also intertwined with the bubble growth dynamics. We explore the bubble growth dynamics using an analytical model. Briefly, the laser-induced heat at the AuNI substrate generates and grows the bubble. The heat dissipation is factored through an efficiency term ( $\eta$ ) in our model. When the liquid is at the saturation temperature, we can assume that the laser-generated heat is used for liquid-to-vapor phase change as per

$$\dot{q}_{\text{vap}} = \dot{m} h_{\text{fg}} \quad (5)$$

where  $\dot{q}_{\text{vap}}$  is the heat associated with bubble formation,  $\dot{m}$  is the mass conversion rate of liquid to vapor, and  $h_{\text{fg}}$  is the latent heat of vaporization.

As detailed in the section “Analytical Modeling of Bubble and Ag Ring Formation” (Supporting Information), we apply the following scaling variables to nondimensionalize the radius of the bubble ( $R_b$ ) and the time ( $t$ )

$$R^* = \left(\frac{1}{r}\right) R_b \quad \text{and} \quad t^* = \left(\frac{3\eta P}{2\rho r h_{\text{fg}}}\right) t \quad (6)$$

As plotted in **Figure 3a**, the evolution of the bubble radius and the growth rate in the nondimensionalized form can be described as

$$R^* = t^{*1/3} \quad \text{and} \quad \frac{dR^*}{dt^*} = \frac{1}{3t^{*2/3}} \quad (7)$$

From **Figure 3a**, we can see that the bubble has a high initial growth rate, which decreases drastically. The Ag NPs are pushed toward the bubble surface due to the high inertial thrust imparted at the instant when the bubble is formed. This explains the absence of Ag NPs around the point of laser incidence and the formation of the Ag rings, as shown in **Figure 2**. The near-instantaneous formation of Ag ring in the silver ink solution without exposure to the ambient atmosphere limits the plausibility of silver oxidation, thereby improving the sample’s shelf life. We observe an increase in the Ag ring radius when the laser power is increased (**Figure 3b** and inset of **Figure 3c**). Our experimental measurements on the power dependence of the ring radius can be explained by the analytical increase of the

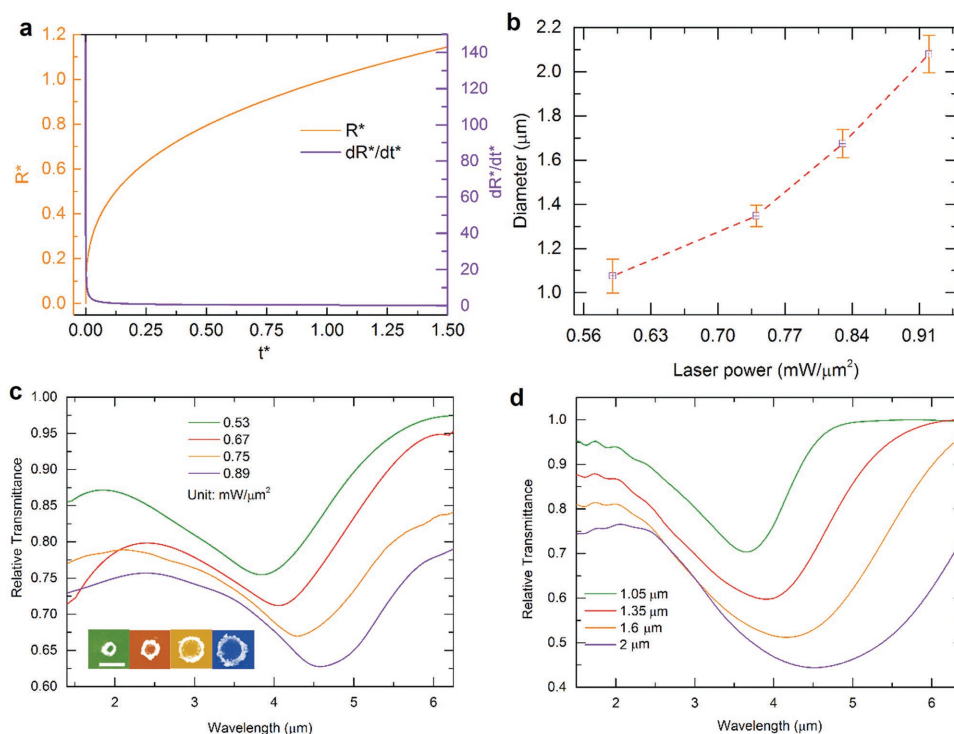


**Figure 3.** a) Calculated temporal evolution of the bubble radius and the growth rate in the nondimensionalized form. b) Measured ring diameter as a function of the incident laser power. c) The relative transmittance spectra of the arrays of Ag rings fabricated at the variable laser power. The spectra were normalized with respect to that of the AuNI substrate as background. The inset shows representative SEM images of four individual rings that increase their diameters (1.08, 1.35, 1.67, and 2.02  $\mu\text{m}$ ) when the incident laser power changes from 0.53 to 0.89  $\text{mW}/\mu\text{m}^2$ . Figure S5a (Supporting Information) denotes the spectra in the visible region. d) The FDTD-simulated relative transmittance spectra for the Ag rings in (c).

bubble radius as a function of  $t^*$  in Figure 3a, which is also proportional to the laser power  $P$  as per the scaling in Equation (6).

The ability to tune the properties of the Ag rings is crucial for their applications.<sup>[36]</sup> We have experimentally established a correlation between the incident laser power and the resultant ring diameter, which can be modulated between  $1.08 \pm 0.07$  and  $2.02 \pm 0.08 \mu\text{m}$  (Figure 3b). The increased ring diameter at the elevated laser power is attributed to the increased bubble size due to the larger amount of vapor generated. A further increase of the laser power causes unstable bubble growth, resulting in a large variation ( $\sigma > 15\%$ ) in the Ag ring diameter. Additional scanning electron microscopy (SEM) and atomic force microscopy (AFM) images of the ring arrays are shown in Figure S3 (Supporting Information). The ring composition is analyzed by EDS mapping. As shown in Figure S3d–f (Supporting Information), Ag is concentrated along the ring and Au is spread out all over the substrate.

We measured the infrared transmission spectra of the variable arrays of Ag rings ( $60 \mu\text{m} \times 50 \mu\text{m}$ ) on the AuNI substrates. Due to the symmetric nature of the Ag ring, there is no dependence on the polarization of the incident infrared beam. As shown in Figure 3c, all the arrays exhibit transmission dips in the mid-infrared regime, which arises from the surface plasmon resonances at the rings. The resonant wavelength varies from 3.8 to 4.6  $\mu\text{m}$  when the Ag ring diameter is increased, as shown in the SEM images in the inset of Figure 3c. A further analysis of the SEM images shows that the ring diameter increases from 1.08 to 2.02  $\mu\text{m}$  and the ring width is between 130 and 200 nm.

We did electromagnetic simulations using finite-difference time-domain (FDTD) method to better understand the experimental optical spectra of the Ag rings. As shown in Figure 3d, the resonant peak wavelength, bandwidth, and symmetry of the simulated spectra are comparable to the experimental data (Figure 3c). A further study of the electric-field distribution at a single Ag ring indicates that the resonance arises from the dipolar plasmon mode (Figure S4, Supporting Information). The resonance tunability of the Ag rings is expected to benefit SEIRA and other sensing applications where a good match between the resonant wavelength and the wavelength of the vibrational mode of the molecular analytes is preferred.

With the visible and infrared surface plasmon resonances that arise from the AuNIs and Ag rings, the Ag ring-AuNI substrate presents an opportunity to achieve dual-mode surface-enhanced optical spectroscopies. We demonstrate SEIRS of TNT and SERS of R6G and CV. As shown in Figure 4a, the aromatic (3.43  $\mu\text{m}$ ) and aliphatic (3.51  $\mu\text{m}$ ) C–H stretch bands of TNT on the Ag ring-AuNI substrate are enhanced via SEIRS.<sup>[25]</sup> The signal enhancements highly depend on the match between vibrational ( $\omega_{\text{vib}}$ ) and plasmonic frequencies ( $\omega_{\text{p}}$ ). No vibrational signal is observed when there is a large frequency mismatch. To further elucidate the plasmon-molecular vibration coupling, we obtain the baseline-corrected SEIRS spectra. As shown in lower panel of Figure 4a, clear Fano-line sharp features appear in the spectra due to the coupling between the vibrational and plasmonic excitations, confirming the SEIRS effect.

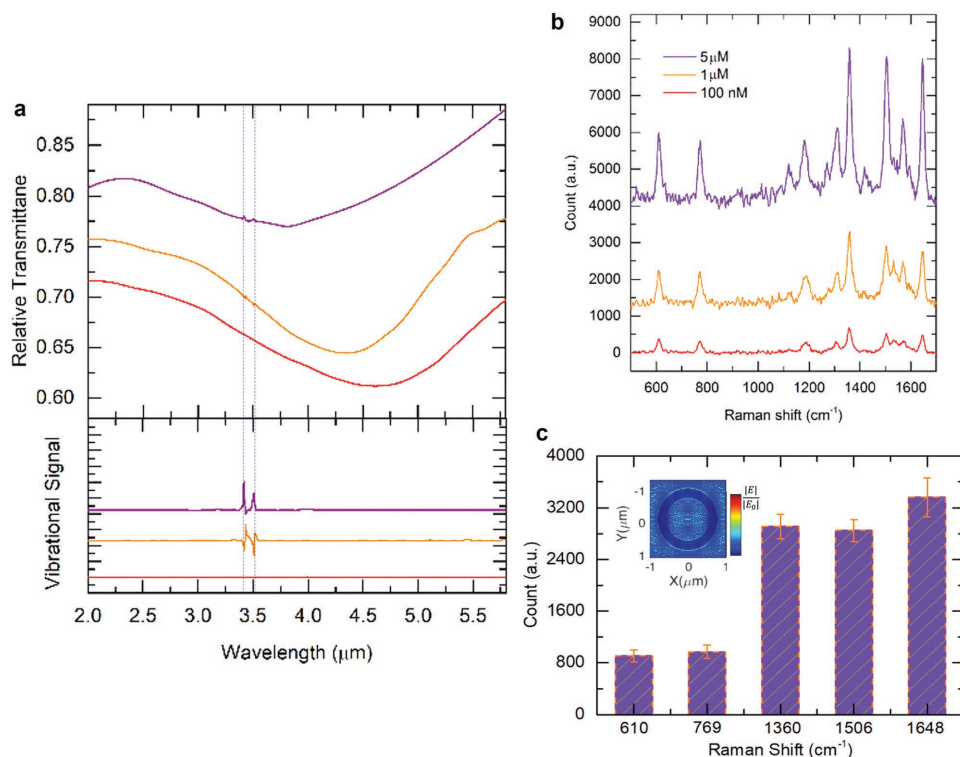


**Figure 4.** a) SEIRS of TNT on three types of the Ag ring-AuNI substrates, which exhibit different detuning between the plasmonic and molecular excitations. The spectra correspond to ring sizes of 1.08, 1.67, and 2.02  $\mu\text{m}$  from top to bottom, respectively. The lower panel shows the baseline-corrected spectra, which clearly reveal the molecular resonances. The baseline was obtained via a second-derivative method. The detuning variation results in the different signal enhancements and lineshapes. b) SERS spectra of R6G of variable concentrations on the Ag ring-AuNI substrate. c) SERS signal counts of the different R6G modes based on multiple spectra taken at various random locations on the sample. The R6G concentration is  $1 \times 10^{-6}$  M. Inset shows the simulated field distributions at the Ag ring-AuNI substrate, which shows the higher field enhancement at the ring interface. The incident laser power was 0.7 mW and the laser beam had a diameter of 2  $\mu\text{m}$ . The Raman acquisition time was 1 s.

We measured the SERS spectra of R6G molecules drop-casted on the Ag ring-AuNI substrate. Figure S5a (Supporting Information) shows the transmission spectrum of the substrate. Figure 4b shows the concentration-dependent SERS spectra with 532 nm incident laser, where distinguishable Raman modes are observed even at the lowest concentration of  $10^{-7}$  M. Many standard modes such as C–C–C ring in-plane bending ( $610\text{ cm}^{-1}$ ), C–C stretching ( $1360$  and  $1506\text{ cm}^{-1}$ ), and C–H bending ( $769$  and  $1648\text{ cm}^{-1}$ ) appear in the spectra.<sup>[37]</sup> Further, we evaluated the Raman enhancement stability across the substrate by measuring multiple spectra at random locations all over the substrate (Figure 4c and Figure S5b, Supporting Information). In general, randomly distributed AuNIs on the substrates do not possess high *E*-field enhancement. Additional steps such as bubble-mediated molecule concentration are often applied to improve the SERS performances on such substrates.<sup>[38]</sup> However, for our hybrid Ag ring-AuNI substrate, we observed a high *E*-field enhancement at the Ag-ring/AuNI interface, as shown in the inset of Figure 4c. The field enhancement arises from the intense hot spots at the multiple Ag–Au junctions with the sub-20 nm gaps. In comparison to the bare AuNI substrate, a tenfold increase in the SERS count is observed for the Ag ring-AuNI substrate (Figure S5c, Supporting Information). The high-resolution Raman mapping

with the  $610\text{ cm}^{-1}$  peak signal also confirms the enhancement at the interfaces (Figure S5d, Supporting Information). Further, the compatibility with 532 nm laser for both fabrication and Raman sensing can be beneficial for device miniaturization via reduced cost and improved throughput. We have also studied the influence of the ring size on the Raman counts (Figure S5e, Supporting Information). The laser was centered on the Ag ring to obtain the spectra. An increase in the counts is observed with increasing radius since the overlap area between Ag ring/AuNI increases from  $\approx 95$  to  $\approx 360\text{ }\mu\text{m}^2$  as the radius increase from 1.08 to 2.02  $\mu\text{m}$ . In addition, we have also demonstrated the sensing of CV at various concentrations, as detailed in Figure S5f (Supporting Information).

The applicability of plasmonic sensors is greatly enhanced by their integration with microfluidic systems.<sup>[17,26]</sup> We demonstrate the “point-and-shoot” in situ fabrication of Ag rings within a microfluidic channel (Video S3, Supporting Information). Due to the noninvasive remote control of light, the light-based synthesis allows us to fabricate Ag rings without any constraints to the channel design and hence is compatible with various on-chip applications.<sup>[39]</sup> Figure S6 (Supporting Information) shows a photo of our microfluidic chip where the AuNIs are confined within the PDMS channel to directly contact the PDMS on the glass substrate for the strong

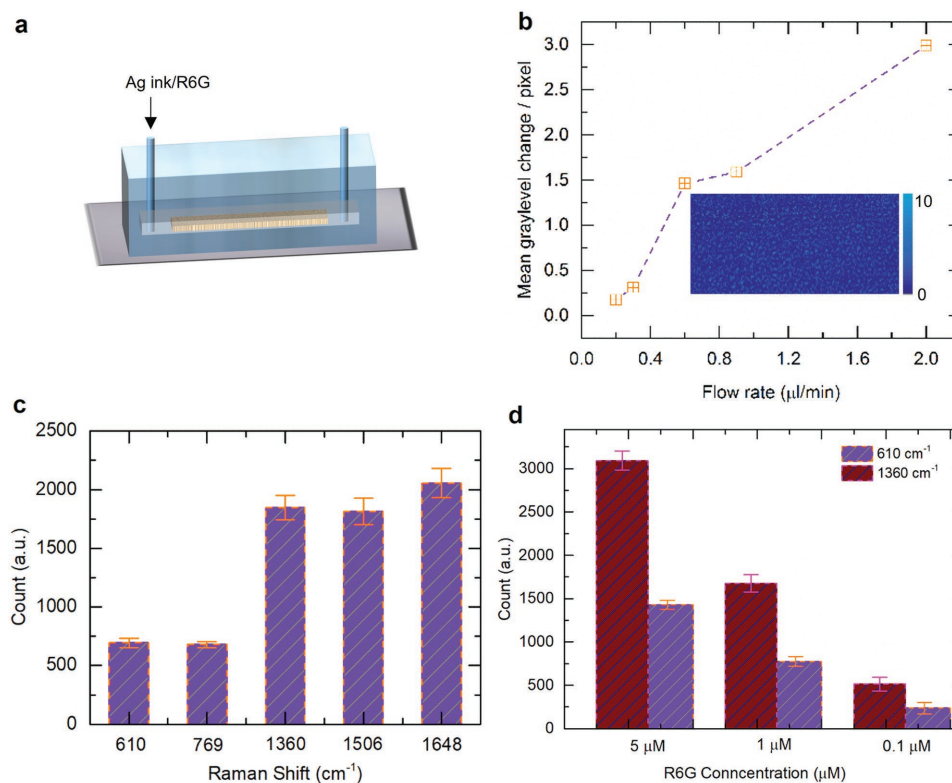


**Figure 5.** a) Schematic of the one-inlet, one-outlet microfluidic setup wherein the silver precursor ink and R6G are introduced sequentially. The microfluidic channel width and height are 500 μm and 80 μm, respectively. b) Plot of the mean pixel change of the optical images taken at various flow rates to demonstrate the stability of the fabricated Ag rings. Inset shows a typical difference image. c) SERS signal counts of the different R6G modes based on many spectra taken at various random locations on the sample with 1.8 μm Ag ring. d) SERS signal counts in the microfluidic chamber as a function of R6G concentration on the sample with 1.8 μm Ag ring.

adhesion. The Ag precursor ink was introduced to the microfluidic channel via the inlet. The fabrication of Ag rings was performed at a laser power of 0.75 mW μm<sup>-2</sup> to yield Ag rings with 1.84 ± 0.11 μm rings. Despite the channel constraint, the laser-generated microbubble induces sufficient flow to concentrate the Ag<sup>+</sup> ions at the bubble interface to form the Ag rings.<sup>[40]</sup> We further evaluate the stability of the Ag rings by analyzing the mean pixel-to-pixel gray level difference ( $\Delta GL_{\text{avg}}$ ) in the control image (0th image) and images obtained at the same location with various flow rates ( $x \mu\text{L min}^{-1}$ ) using the following equation

$$\Delta GL_{\text{avg}} = \frac{1}{m+n} \sum_{i=0}^m \sum_{j=0}^n GL_{x,i,j} - GL_{0,i,j} \quad (8)$$

where the images have  $m \times n$  pixels. The typical mean difference is  $\leq 3$  at the various flow rates, demonstrating the high stability of the Ag rings (inset of **Figure 5b** and **Figure S7**, Supporting Information).

Finally, we demonstrate in situ SERS of R6G molecules based on the Ag ring-AuNI substrate in the microfluidic channel. The channel was thoroughly cleaned with DI water prior to the introduction of R6G solution. **Figure 5c** shows the SERS signal counts of the different R6G ( $1 \times 10^{-6}$  M) modes based on many spectra taken at various random locations of the

substrate within the channel, revealing the spatially uniform and repeatable measurements. Further, the SERS spectra at various concentrations of R6G from  $5 \times 10^{-6}$  to  $100 \times 10^{-9}$  M were obtained (**Figure 5d**). A similar decreasing trend with reducing concentration was observed. However, the standard deviation of the counts was reduced by  $\approx 35\%$  owing to the even distribution of analyte molecule.

In summary, the laser-induced bubble printing enables “point-and-shoot” one-step synthesis of Ag rings for surface-enhanced optical spectroscopies. The technique is applicable to microfluidic systems with spatial constraints. The ring fabrication benefits from the low-temperature reducible Ag precursor ink, the AuNI substrate that provides highly localized temperature increase upon the laser irradiation, and the high inertial thrust imparted at the instant when the bubble is formed. The high temperature and convection-mediated Ag<sup>+</sup> ion concentration at the three-phase line enable ultrafast Ag particle synthesis and immobilization at high spatial resolution. With their tunable plasmon resonances in the visible and infrared regimes, the hybrid Ag ring-AuNI substrates have been applied for SERS and SEIRS of R6G, CV, and TNT, respectively. With its simplicity, high-efficiency, and integrability in fabrication of micro/nanostructures, our “point-and-shoot” approach paves the way toward device miniaturization, portability, and multifunctionality.

## Experimental Section

A detailed description of procedures, characterization methods, simulation, and analytical modeling are available in the Supporting Information.

## Supporting Information

Supporting Information is available from the Wiley Online Library or from the author.

## Acknowledgements

Y.Z. acknowledges the financial supports of the Early Career Faculty Award from National Aeronautics and Space Administration (80NSSC17K0520) and of the Army Research Office (W911NF-17-1-0561). S.R.B. acknowledges the financial support from the National Science Foundation (NSF-ECCS-1408302). V.B. acknowledges NSF-CBET Grant No. 1605789 for partial support of this work. The Texas Advanced Computing Center (TACC) at The University of Texas at Austin provided HPC resources that contributed to the research results reported in this paper (<http://www.tacc.utexas.edu>).

## Conflict of Interest

The authors declare no conflict of interest.

## Keywords

Ag rings, multiresponsive plasmonic substrate, plasmonic microbubbles, surface-enhanced infrared spectroscopy, surface-enhanced Raman spectroscopy

Received: November 14, 2017  
Revised: February 6, 2018  
Published online: March 8, 2018

- [1] N. Meinzer, W. L. Barnes, I. R. Hooper, *Nat. Photonics* **2014**, *8*, 889.
- [2] P. Nordlander, *ACS Nano* **2009**, *3*, 488.
- [3] J. Aizpurua, P. Hanarp, D. S. Sutherland, M. Kall, G. W. Bryant, F. J. G. de Abajo, *Phys. Rev. Lett.* **2003**, *90*, 057401.
- [4] J. Ye, P. Van Dorpe, L. Lagae, G. Maes, G. Borghs, *Nanotechnology* **2009**, *20*, 465203.
- [5] E. M. Larsson, J. Alegret, M. Kall, D. S. Sutherland, *Nano Lett.* **2007**, *7*, 1256.
- [6] A. E. Cetin, H. Altug, *ACS Nano* **2012**, *6*, 9989.
- [7] M. G. Banaee, K. B. Crozier, *Opt. Lett.* **2010**, *35*, 760.
- [8] F. Hao, Y. Sonnefraud, P. Van Dorpe, S. A. Maier, N. J. Halas, P. Nordlander, *Nano Lett.* **2008**, *8*, 3983.
- [9] C. J. Huang, J. Ye, S. Wang, T. Stakenborg, L. Lagae, *Appl. Phys. Lett.* **2012**, *100*, 173114.
- [10] Z. A. Lewicka, Y. Li, A. Bohloul, W. W. Yu, V. L. Colvin, *Nanotechnology* **2013**, *24*, 115303.
- [11] J. Zhao, B. Frank, F. Neubrech, C. J. Zhang, P. V. Braun, H. Giessen, *Beilstein J. Nanotechnol.* **2014**, *5*, 577.
- [12] B. B. Rajeeva, Y. B. Zheng, *Nanotechnology* **2016**, *27*, 23.
- [13] F. Neubrech, C. Huck, K. Weber, A. Pucci, H. Giessen, *Chem. Rev.* **2017**, *117*, 5110.
- [14] Y. Babayan, J. M. McMahon, S. Z. Li, S. K. Gray, G. C. Schatz, T. W. Odom, *ACS Nano* **2009**, *3*, 615.
- [15] D. L. Sounas, A. Alu, *ACS Photonics* **2014**, *1*, 198.
- [16] B.-B. Xu, R. Zhang, X.-Q. Liu, H. Wang, Y.-L. Zhang, H.-B. Jiang, L. Wang, Z.-C. Ma, J.-F. Ku, F.-S. Xiao, *Chem. Commun.* **2012**, *48*, 1680.
- [17] O. Tokel, F. Inci, U. Demirci, *Chem. Rev.* **2014**, *114*, 5728.
- [18] J. Chen, W.-S. Liao, X. Chen, T. Yang, S. E. Wark, D. H. Son, J. D. Batteas, P. S. Cremer, *ACS Nano* **2008**, *3*, 173.
- [19] A. R. Halpern, R. M. Corn, *ACS Nano* **2013**, *7*, 1755.
- [20] Y. Bao, T. A. Witten, N. F. Scherer, *ACS Nano* **2016**, *10*, 8947.
- [21] Y. Zheng, S. Wang, A. Huan, Y. Wang, *J. Non-Cryst. Solids* **2006**, *352*, 2532.
- [22] R. Winkler, F.-P. Schmidt, U. Haselmann, J. D. Fowlkes, B. B. Lewis, G. Kothleitner, P. D. Rack, H. Plank, *ACS Appl. Mater. Interfaces* **2016**, *9*, 8233.
- [23] A. B. Taylor, P. Michaux, A. S. Mohsin, J. W. Chon, *Opt. Express* **2014**, *22*, 13234.
- [24] O. Wolf, S. Campione, A. Benz, A. P. Ravikumar, S. Liu, T. S. Luk, E. A. Kadlec, E. A. Shaner, J. F. Klem, M. B. Sinclair, *Nat. Commun.* **2015**, *6*, 7667.
- [25] S. Bagheri, K. Weber, T. Gissibl, T. Weiss, F. Neubrech, H. Giessen, *ACS Photonics* **2015**, *2*, 779.
- [26] Y. Xie, S. Yang, Z. Mao, P. Li, C. Zhao, Z. Cohick, P.-H. Huang, T. J. Huang, *ACS Nano* **2014**, *8*, 12175.
- [27] B. J. Roxworthy, K. D. Ko, A. Kumar, K. H. Fung, E. K. C. Chow, G. L. Liu, N. X. Fang, K. C. Toussaint, *Nano Lett.* **2012**, *12*, 796.
- [28] L. H. Lin, X. L. Peng, Z. M. Mao, W. Li, M. N. Yogeesh, B. B. Rajeeva, E. P. Perillo, A. K. Dunn, D. Akinwande, Y. B. Zheng, *Nano Lett.* **2016**, *16*, 701.
- [29] B. Bangalore Rajeeva, L. Lin, E. P. Perillo, X. Peng, W. W. Yu, A. Dunn, Y. Zheng, *ACS Appl. Mater. Interfaces* **2017**, *9*, 16725.
- [30] B. B. Rajeeva, M. A. Alabandi, L. Lin, E. P. Perillo, A. K. Dunn, Y. Zheng, *J. Mater. Chem. C* **2017**, *5*, 5693.
- [31] S. Fujii, R. Fukano, Y. Hayami, H. Ozawa, E. Muneyuki, N. Kitamura, M. Hag, *ACS Appl. Mater. Interfaces* **2017**, *9*, 8413.
- [32] S. B. Walker, J. A. Lewis, *J. Am. Chem. Soc.* **2012**, *134*, 1419.
- [33] M. Enders, S. Mukai, T. Uwada, S. Hashimoto, *J. Phys. Chem. C* **2016**, *120*, 6723.
- [34] R. P. Sear, *J. Phys.: Condens. Matter* **2007**, *19*, 033101.
- [35] C. L. Zhao, Y. L. Xie, Z. M. Mao, Y. H. Zhao, J. Rufo, S. K. Yang, F. Guo, J. D. Mai, T. J. Huang, *Lab Chip* **2014**, *14*, 384.
- [36] S. Aksu, A. E. Cetin, R. Adato, H. Altug, *Adv. Opt. Mater.* **2013**, *1*, 798.
- [37] L. Jensen, G. C. Schatz, *J. Phys. Chem. A* **2006**, *110*, 5973.
- [38] Z. W. Kang, J. J. Chen, H. P. Ho, *Nanoscale* **2016**, *8*, 10266.
- [39] P. Y. Chiou, A. T. Ohta, M. C. Wu, *Nature* **2005**, *436*, 370.
- [40] Y. L. Xie, C. L. Zhao, Y. H. Zhao, S. X. Li, J. Rufo, S. K. Yang, F. Guo, T. J. Huang, *Lab Chip* **2013**, *13*, 1772.